

Earth and Space Science



RESEARCH ARTICLE

10.1029/2018EA000403

Special Section:

Planetary Mapping: Methods,
Tools for Scientific Analysis
and Exploration

Key Points:

- We present an open source code to generate illumination maps of Mars
- The code can be used for geomorphological and energy analysis
- Analysis of illumination of Mars' terrains in low computational times

Correspondence to:

M. G. Spagnuolo,
mgspeg@gmail.com

Citation:

Spagnuolo, M. G., Carballo, F. D.,
Marco Figuera, R., & Rossi, A. P. (2019).
MarsLux: HI-resolution illumination
maps generator for Mars. *Earth and
Space Science*, 6, 146–155. [https://doi.
org/10.1029/2018EA000403](https://doi.org/10.1029/2018EA000403)

Received 16 APR 2018

Accepted 19 DEC 2018

Accepted article online 5 JAN 2019

Published online 30 JAN 2019

©2019. The Authors.

This is an open access article under the terms of the Creative Commons Attribution-NonCommercial-NoDerivs License, which permits use and distribution in any medium, provided the original work is properly cited, the use is non-commercial and no modifications or adaptations are made.

MarsLux: HI-Resolution Illumination Maps Generator for Mars

M. G. Spagnuolo¹ , F. D. Carballo², R. Marco Figuera³ , and A. P. Rossi³ ¹IDEAN, Universidad de Buenos Aires, Conicet, Buenos Aires, Argentina, ²SEGEMAR, Buenos Aires, Argentina, ³Department of Physics and Earth Sciences, Jacobs University Bremen, Bremen, Germany

Abstract Illumination simulation codes for the Moon's surface have been thoroughly developed during the last years. Despite works done for the Moon, no studies have investigated the relation between sunlight illumination and the Martian surface applying those codes done for the Moon to Mars. The objective of this work is to describe the development of a surface illumination simulation code, called MarsLux, which allows users to make a detailed investigation of the illumination conditions on Mars, based on its topography and the relative position of the Sun. Our code can derive accurate illumination maps, from topographic data, showing areas that are fully illuminated, areas in total shadow, and areas with partial shade, in short computational times. Although the code does not take into account any atmospheric effect, the results proved to be of high accuracy. The maps generated are useful for geomorphological studies, to study gullies, thermal weathering, or mass wasting processes as well as for producing energy budget maps for future exploration missions.

1. Introduction

One key technological challenge for future human and robotic space exploration to distant locations from Earth is the efficient generation of energy. Solar panels were used among most planetary missions, especially in rovers, since the replacement of Radioisotope Radiation Units (Carpenter et al., 2012). Nevertheless, this change has opened a range of challenges to be solved. As a consequence, a whole field of studies in the calculation of illumination on the surface of the Moon and its behavior was carried out. Those studies were focused in thermal properties (Bussey et al., 1999), planetary missions, especially landers (Speyerer & Robinson, 2013), and for future human missions (e.g., Gläser et al., 2014, and references therein; Sherwood, 2017; Stenzel et al., 2018). The illumination analyses are also important to study geomorphological processes like rock weathering (Wu & Hapke, 2018) or, in the case of Mars, the evolution of gullies and ice melting processes (Kolb et al., 2010; Raack et al., 2015).

Illumination simulation codes for the Moon's surface have been thoroughly developed during the last years (Gläser et al., 2014; Mazarico et al., 2011; Noda et al., 2008; Speyerer & Robinson, 2013). Despite the good results, the development of the different techniques used to analyze light conditions is not straightforward. The most important obstacle to overcome is the large computational times involved in the process.

Despite the amount of work done for the Moon, few studies have investigated the relation between sunlight illumination and the Martian surface. Planned missions to send humans to the Mars' surface (MEPAG, 2015), by many nations and organizations, have opened a new interest in the study of surface illumination. Moreover, the geomorphological studies, together with an analysis of the energy budget of the area of interest, would take part in the strategic decision of future emplacement of human colonies. Not only is the energy issue of importance but also the geological and geomorphological aspects—for example, the presence of local water sources (Dundas et al., 2018), as well as the origin of recurring slope lineae (Garcia-Chevesich et al., 2017).

The objective of this work is to describe the development of a surface illumination simulation code, called MarsLux, which allows users to make a detailed investigation of the illumination conditions on Mars, based on its topography and the relative position of the Sun (Figure 1).

The studies conducted by Noda et al. (2008) and Bussey et al. (2010) were based in the ray-tracing method. In recent investigations carried out by Mazarico et al. (2011) and De Rosa et al. (2012), the method used was

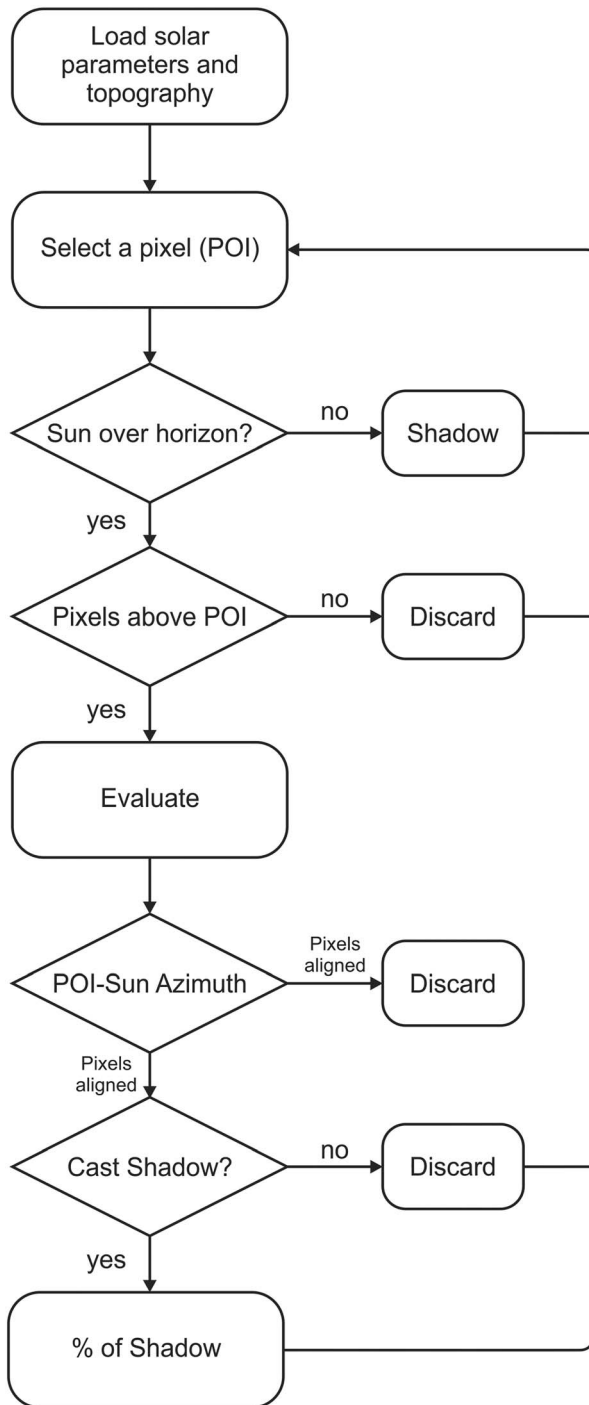


Figure 1. MarsLux flowchart.

called “horizon method.” The main difference to the ray-tracing method is that, for each pixel in the region of interest (RoI), a horizon is calculated and stored as the maximum elevation in different azimuthal directions. While Margot et al. (1999), Noda et al. (2008) and Bussey et al. (2010) used the ray-tracing method to derive the illumination conditions at a given time. Mazarico et al. (2011) found advantages by using the so-called horizon method, which becomes especially effective when looking at the same site over longer time scales involving many time steps. Later, the horizon method was improved by implementing parallel programming computations in either CPUs and/or GPUs (Gläser et al., 2014; Marco Figuera et al., 2014).

Our scope here is to present a code, fast enough, without using parallel computation, to be run in a desktop computer by nonspecialized users, allowing them to use it as a tool for research, targeting geomorphologic applications. This algorithm is a mix between the ray-tracing method, giving that the whole elevation computation and visible solar-disk calculation is achieved in one step, and the horizon method, since the code works with the points that only can potentially cast shadows. All the calculations are made considering Mars as an airless body, and no atmospheric effects are taken into account. The codes SolaPar and MarsLux will be available to the public (DOI:10.5281/zenodo.1215719).

2. Data and Methods

To analyze the distribution of lit or shadowed areas on the surface of Mars, we developed a code based on the geometric relationship between the position of the Sun, a Point of Interest (PoI) on the surface and its surrounding topography. The code simulates the illumination conditions over a given time period. The simulation is divided into three steps: the first step comprises the calculation of the Sun position; followed by the evaluation of light conditions; and finally, estimating the different statistical parameters of the amount of light and energy.

2.1. Sun Position

The parameters of Sun position required for the illumination analysis were obtained following the works presented by Allison (1997) and Allison and McEwen (2000).

The main parameters used to calculate the shadows are the areocentric solar longitude calculated with equation (1):

$$L_s = \alpha FMS + (v - M) \tag{1}$$

αFMS is the angle of Fiction Mean Sun and $v - M$ is the equation of center. Then the Solar declination δ_s is calculated with equation (2):

$$\delta_s = \sin^{-1}[0.42565 * \sin(L_s)] * 0.25 * \sin(L_s) \tag{2}$$

L_s represent the areocentric longitude obtained in equation (1). Equation (3) corresponds to the Mars-Sun distance, which represents the distance from the center of Mars to the center of the Sun:

$$RM = 1.52367934 * [1.00436 - 0.09309 * \cos(M) - 0.004336 * \cos(2 * M) - 0.00031 * \cos(3M) - 0.00003 * \cos(4M)] \quad (3)$$

Using equation (4), we obtained the Sun's azimuth:

$$A = \tan^{-1} \left(\frac{\sin H}{(\cos \varphi \tan \delta s - \sin \varphi \cos H)} \right) \quad (4)$$

where H is the “hour angle” and φ is the planetographic latitude. Finally, the solar elevation is obtained from equation (5), which is calculated as the angle from the zenith where 90 is the horizon:

$$Z = \cos^{-1}[\sin(\delta s) * \sin(\varphi) + \cos(\delta s) * \cos(\varphi) * \cos(H)] \quad (5)$$

The input for this step is a grid of Latitudes and Longitudes of the Region of Interest (RoI). Then, an initial and final dates are required in order to calculate the parameters between that period which can be one particular date (assuming the same initial and final date) or a larger lapse of time.

A matrix of the same size of the Latitudes and Longitudes is obtained for each one of the parameters mentioned above at one given time. These matrices are obtained with periodic time steps that can be established by the user, in hours, between the initial and the final required dates (e.g., every 12 hr).

2.2. Evaluation of Light Conditions

The second step of the process is the evaluation of light conditions taking into account the surrounding topography. We use the matrices of the Sun parameters, previously obtained for each time step, together with a Digital Terrain Model (DTM) of the RoI.

The process is based on the analysis of the line of sight between the PoI (i,j) and each surrounding topographic points, with respect to the Sun position. This process is repeated for each pixel of the DTM, and because of that, it is a very time-consuming computation process. To make the process faster we apply filters to avoid evaluating points of the DTM that we know the result in advance. For example, we search for points in the night side, assigning a value of 0 to them. We also reduce the initial DTM to submatrices in order to only evaluate the minimum number of pixel, for example, not evaluating the point opposite to the Sun's azimuth or the points that are below PoI.

Map distances between the PoI and any other point of the grid are measured using Pythagoras' theorem on an equirectangular approximation (equations (6)–(8); Snyder, 1987). Despite the errors that can generate this projection in long distances, we find it useful for small areas, and simply to implement with good results when working in low latitudes. Moreover, the azimuth lines are represented as straight lines.

$$x = [\text{Lon} - \text{Lon}(i,j)] * \cos \left[\frac{\text{Lat} + \text{Lat}(i,j)}{2} \right] \quad (6)$$

$$y = \text{Lat} - \text{Lat}(i,j) \quad (7)$$

$$d = \sqrt{(x^2 + y^2)} * R \quad (8)$$

The height differences also need to be corrected for the curvature of the sphere concerning the distance from the PoI by equation (9), where E is the elevation, d is the distance obtained from equation (8), and R is the Mars radius.

$$Ec = E - \frac{d^2}{2 * R} \quad (9)$$

After all the corrections are applied, the script starts at the first pixel and transforms each elevation value to an Angle of Sight (AoS; α) from the PoI using simple trigonometric relation (equation (10)).

$$\alpha = \tan^{-1} \left[\frac{Ec - Ec(i,j)}{d} \right] \quad (10)$$

where $Ec - Ec(i,j)$ is the difference in height between each pixel and the PoI and d is the distance between the points from equation (8). Then, the (α) values are compared to the solar elevation. We will call this a vertical

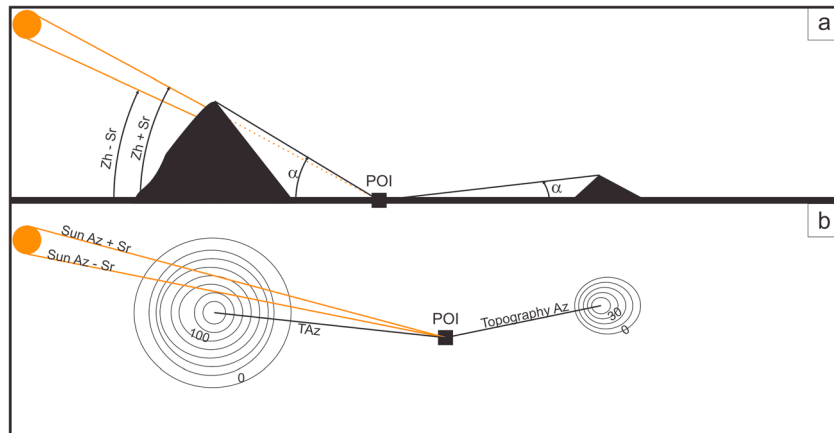


Figure 2. Conceptual scheme used for the analysis. (a) Sketch depicting the vertical analysis. The angle of sight (AoS) from the point of interest (PoI) to each pixel on the DTM is represented by “ α .” In the example, the solar elevation angle (Zh) plus the solar radii (Sr) is below the AoS, thus casting a shadow. (b) Sketch depicting the horizontal analysis (map view). The azimuth from the PoI to each pixel on the DTM (TAz) is compared with the Sun’s maximum (sun Az + Sr) and minimum azimuth (sun Az – Sr). In this case, the azimuth to the pixel is outside the range of solar disk azimuths, resulting in an illuminated PoI.

analysis (Figure 2a). For the vertical analysis, we do not consider the pixels for which its angle of sight is negative from the PoI’s view. Only those points that have a positive (α) are compared with the solar elevation angle. If the AoS results bigger than the solar elevation plus the Sun’s radii (Zhmax), the PoI is in the shade (Figure 2a). Otherwise, we calculate how much quantity of Sun is seen by the PoI taking in account the difference between the upper edge of the Sun (Zhmax) and the AoS (α) and the solar radii using equation (11).

$$SV(i,j) = \frac{Zh_{max} - \alpha}{2 * S_{disc}(i,j)} \quad (11)$$

The resultant shadow is expressed as a percentage, proportional to the diameter of the apparent Sun, and the value is later stored as the vertical analysis result.

After the vertical analysis result, the script proceeds with the horizontal analysis based on the azimuthal location of the Sun. This horizontal analysis is done similarly as the vertical analysis but using the azimuthal angle. Here we only evaluate the pixels that are located in the solid angle formed by the solar radii on edge, and the PoI as the opposite vertex. The code compares the azimuth from the PoI to each point on the DTM (TAz), and then, those values are compared with the solar azimuth (SunAz; Figure 2b). If the Taz value is in the range of the azimuth to the Sun, the proportion of visible Sun is estimated. Finally, the total amount of light, received by the PoI, is the outcome obtained by multiplying the vertical and horizontal results (Figure 3). It has been established 0 for total shadow and 1 for full light. The result is stored in a matrix for each hour or any time interval analyzed.

2.3. Energy Calculation

The final part of the code allows the user to compute several statistical parameters to quantify the amount of light and energy received by each pixel, within the RoI, in the established period. The parameters obtained are the total number of hours of full light, the daily accumulated amount of light intensity, the daily maximum light intensity, and a daily average of light intensity. All these parameters can be computed, also weekly and yearly, if needed. The light intensity is obtained by equation (12).

$$S_i = S_o * \cos(Z) * \left[\left(\frac{1.52}{D} \right)^2 \right] \quad (12)$$

where S_i represents the light intensity in W/m^2 ; S_o is the solar irradiance at the Mars’ mean distance from the Sun (1.52 AU), which is $590 W/m^2$; Z is the solar zenith angle; and D is the Mars-Sun distance. The

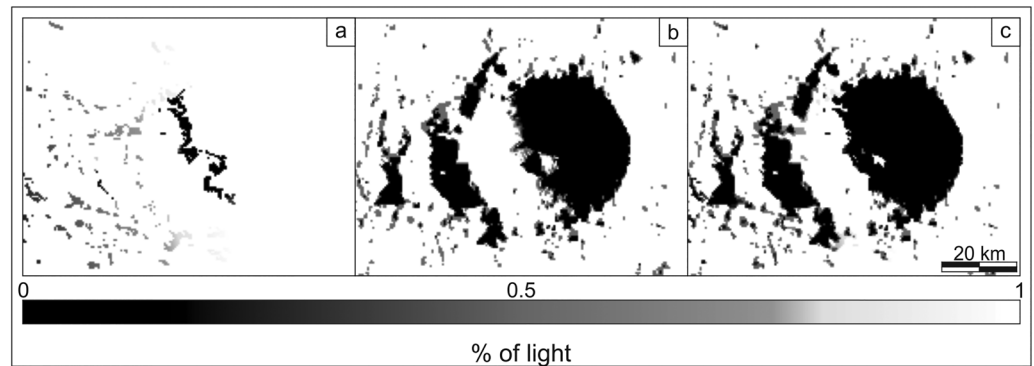


Figure 3. The figure shows illumination conditions for the Toro crater where the Sun is at an azimuth of 64.5° , and a solar elevation angle of 4.8° . Scale bar at the bottom shows a percentage of shade between total darkness (0) and full light (1). (a) Outcome of the horizontal analysis. (b) Outcome of the vertical analysis. (c) Final result of percentage of shadow from the combination of (a) and (b).

energy value does not take into account any atmospheric correction, and does not discriminate between different wavelengths. The daily average of energy is expressed in kilowatts per hour per area (kWh/m^2), which is used in solar power estimations (Acton, 1996).

3. Results

In this section, we will describe the performance and results of the code. In order to do this, we run a test to evaluate the performance of the code with a simulated topography. We also tested the computational times, using DTMs of the same area with different spatial resolutions. Finally, the code was validated comparing the results with real cases.

To test how the code responds to different Sun's positions (azimuth and solar elevation), we generated a mock topography with simple geometrical features. This DTM consisted of a flat surface of $3,476 \text{ km}^2$, with three 3-D geometric features with a resolution of 160 m/pixel . Martian coordinates were assigned to the DTM to simulate real conditions. One of the features was a pyramid, another one a truncated cone, and the third one a Gaussian cone. All the three promontories have approximately a high of about 2.3 km .

We run eight simulations changing the azimuth of the Sun, with the same solar elevation, every 45° . Figure 4 shows the results of the simulations. As the Sun moves around the features, the shadow follows the movement. Also, the shape of the shadows varies according each geometrical feature. The match between the shadow and the features is, particularly, observed between the shadows of the truncated and Gaussian cone. Moreover, the lengths of the shadows have the correct distance considering the relation between the features' high and the solar elevation angle. For example, using the simple relation of $D_s = H/\tan(Z_h)$, where D_s is the length of the shadow, Z_h is the solar elevation angle, and H is the height of the feature, we can estimate that the shadow's length for the pyramid with $H = 1,994 \text{ m}$ and $Z_h = 16.8^\circ$ results in a shadow length of 6.6 km while the simulation estimates a value of 6.5 km . This small difference can be due to the curvature correction, which is applied in the simulation, and the size of the pixels.

After the positive results of the initial analysis, we tested the computational time of the code. This test was performed using a HiRISE DTM (DTEEC_002446_1700_001602_1700_U01) obtained from <https://www.uahirise.org/>, centered at $9^\circ 54'S$ and $91^\circ 51'W$, with an area of 0.355 km^2 (Kirk et al., 2008; McEwen et al., 2007). The area is dominated by a central peak with a maximum height difference of 300 m which ensured the presence of shadows in the analysis. The time test was performed using different spatial resolutions, squared pixel sizes of $1.00, 1.16, 1.58, 2.63, \text{ and } 5.27 \text{ m}$ for the same Sun conditions. Time results are shown in Figure 5, where it can be observed that computational time increases with the number of analyzed pixels, following a quadratic relation. The difference of time consumed, increasing the spatial resolution by a factor

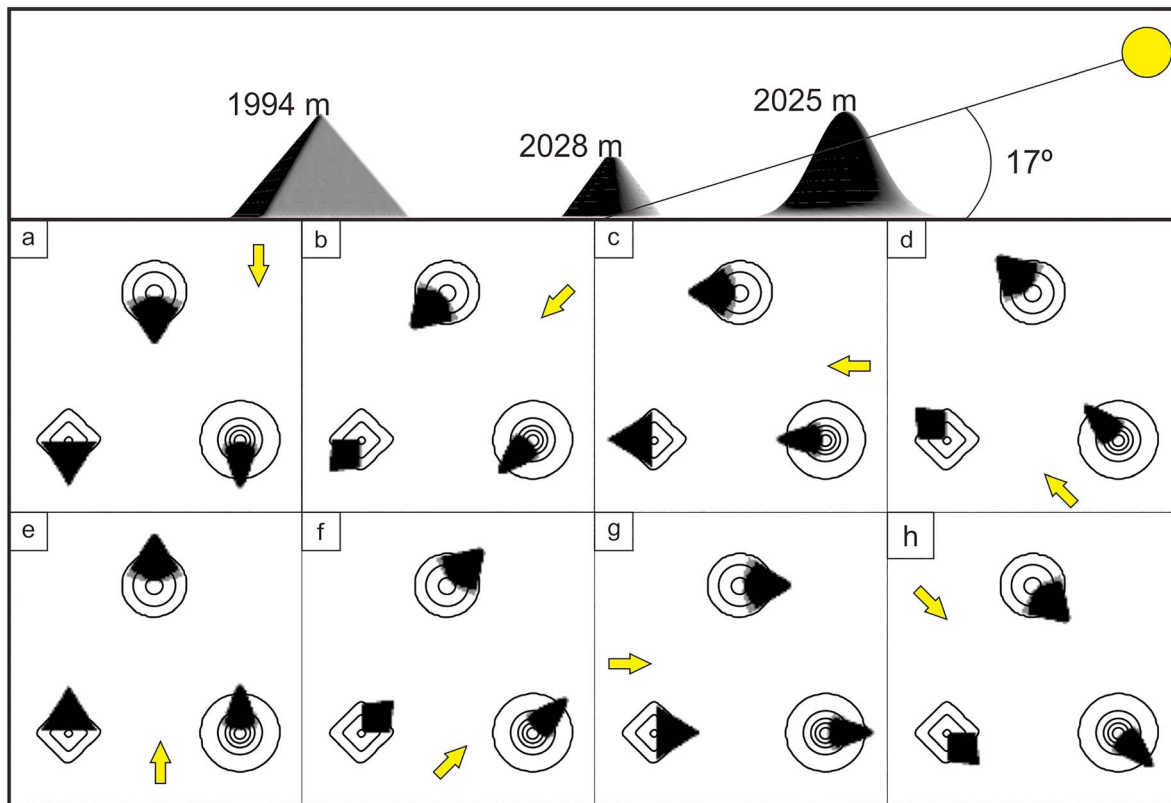


Figure 4. (a–d) A perspective view of the topography with the solar elevation value, together with the height of each feature in km. (e–h) The sequence of the results simulating the sun rotation between an azimuth 0° in (a) to 315° in (h). The shadows are overlapping contour line maps.

of 2, from 5.27 to 2.63 m/pixel, is not significant. On the other hand, when the pixel reaches a critical high resolution, a small decrease in size implies a dramatic increment of time.

Final validation of the code was performed comparing illumination simulations of Mars real terrains, with optical images of the same areas.

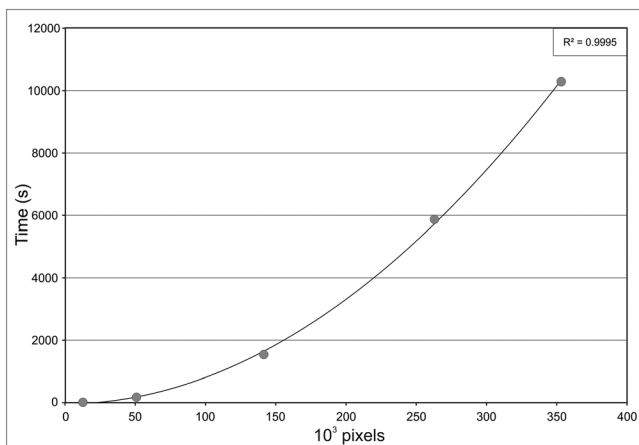


Figure 5. The figure shows the relation between processing time and the total number of pixels of a DTM. The observed relation observed adjusts to a quadratic regression, being possible to estimate the time required to evaluate a certain area, given a particular resolution.

We selected images of three different locations covering north and south hemispheres and different longitudes (Table 1). The corresponding DTMs for the three areas were subsampled to a resolution of 10 m/pixel. The date and time, used as input for the simulations, were obtained from the start time of acquisition of the images, available in the metadata (see Table 1).

Figure 6 shows the comparison between the HiRISE product (centered in the red band) and the result illumination maps from the simulations. Note that the resolution difference between the HiRISE images and the simulated illumination maps are in the range of 20 to 40 times smaller (0.25–0.5-m/pixel HiRISE image and 10-m/pixel subsampled DTMs). As will be discussed later, this is one of the factors of discrepancy between reality and simulated maps. Despite this, the comparison of simulated data with ground truth reveals that even very small surface features, of just a few pixels, are reproduced in the simulation, showing zones of full light, partial, and total shadows. Hence, accurate illumination maps can be obtained from the DTMs. Nevertheless, some few discrepancies are observed due to the intrinsic problem of using a DTM with square pixels and, especially, by using a subsampled DTM.

Table 1
Properties of the Data Set Used in Figure 6

Image	ESP_022217_1440	ESP_036375_1975	PSP_002446_1700
Date	05 March 2011	30 April 2014	03 February 2007
Location	33°S, 24°E	17°N, 126°W	10°S, 91°W
Solar elevation (deg)	45.65	40.35	35.36
Local time (hr)	15.30	15.51	15.58
Solar longitude (deg)	248.43	123.97	177.34
Solar azimuth (deg)	272.18	282.50	278.45

The accuracy of the results can be improved using higher-resolution DTMs but also the processing time will increase by orders of magnitude. Nevertheless, it is possible to do detail studies of small areas using very high-resolution data sets. Figure 7 shows a detail simulation using the HiRISE DTM DTEEC_002446_1700_001602_1700_U01 resampled to 1-m/pixel resolution. The area is close to the center of Figure 6b. This outcome was obtained in less than 3 hr, using a desktop computer with a CPU of 8 cores of 3.6 Ghz and 16 Gb of RAM. Note that the real shadows as not as deep as the simulated ones, probably caused by atmospheric effects and by surface reflections, which are not considered in the code.

4. Discussion

The results of the calculations prove to be accurate and fast for medium- and low-resolution DTMs. Some of the pitfalls of the method are linked the dependency between the computational time and the number of pixels of the analyzed area, similar to the ray-tracing method (Noda et al., 2008, Bussey et al., 2010).

Another problem is the discretization of the topography. Each pixel has a particular dimension and altitude value, but the azimuth of the line between the PoI and the other pixels are computed from center to center. This is particularly problematic with the adjacent pixel to the PoI resulting in large variations in azimuths between the center of the pixel and the edges, causing that pixels that are in the line of sight to the Sun could be discarded as possible casters of shadow. We take into account this problem and the pixel size is evaluated when comparing with the solar azimuth and radii.

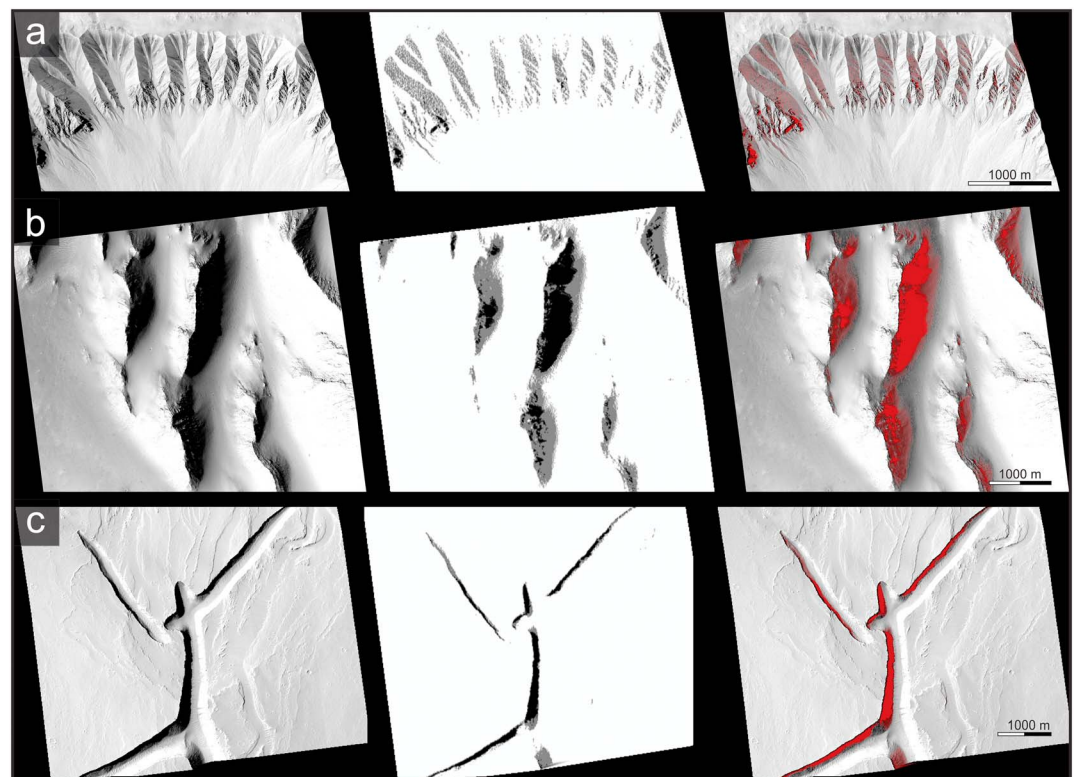


Figure 6. The figure shows the results of the simulation for the three example areas. HiRISE images are shown on the left. Illumination simulated maps are shown in the middle, and on the right, the simulated map is superposed to the HiRISE images. (a) Section of the ESP_022217_1440 image, (b) section of the PSP_002446_1700 image, and (c) section of ESP_036375_1975 image.

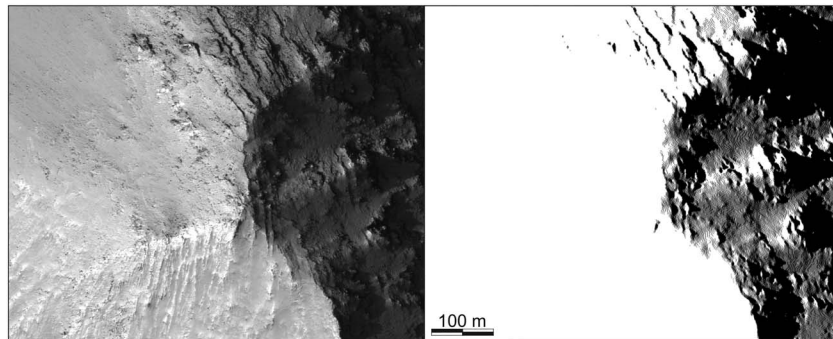


Figure 7. The figure shows a comparison between a portion of HiRISE image PSP_002446_1700 (left) and the simulated illumination map for the same area (right).

Another problem of working with discretized DTMs is that they can only make an approximation of the real topography. High-resolution DTMs can generate better outcomes resulting in a very time-consuming process. While smoothing of the topography can accelerate the process, the chances of pixels to produce shadows or generate artifacts are increased. One possible solution to generate less PoIs to analyze is to work with RTINs (Evans et al., 2001; Marks et al., 2017). Since the RTINs can generate data sets with differential resolution, a large area can have low number of point in some smooth zones and more points in irregular zones. Moreover, using RTINs can be helpful to get the normal vector of each facet and improve the results taking in account internal reflections. Despite the benefits of using TINs the approach of the code presented here is not compatible and would require a completely different analysis.

The speed issues are caused by the fact that, for each PoI, the code has to evaluate several amounts of pixels and terrain complexity. Nevertheless, since each PoI evaluation is independent, the script can be parallelized (Marco Figuera et al., 2014). Marco Figuera et al. (2014) GPU parallel code can process a 10,000-pixel area over one year of Mars in 25 s, while with our approach the same amount of pixels consume near 34 hr.

The dust aerosol plays a key role in the opacity of the Martian atmosphere (Chen-Chen et al., 2019) and global dust storms occur episodically (Strausberg et al., 2005). As mentioned before, the code does not take in account any of those atmospheric effects, so in some cases, the shadows simulated are deeper than in reality and, in others, there will be shadows generated by clouds that would not be considered.

Despite all the performance flaws commented above, the presented approach has the potential, not only to be used for research of energy budgets in specific landing areas but also for several geological studies of the relationship between geomorphological processes and illumination. Moreover, it can be useful to analyze areas with permanent ice and possible water sources. This type of code can help to understand the formation of slope streaks, gullies, and recurring slope lineae. Garcia-Chevesich et al. (2017) suggested that RSL are part of weathering processes, in which the constant freezing and thawing of water during Martian summer nights and days generate them. On the other hand, Núñez et al. (2016) argued that there is no clear indication of long-lived liquid water to have a role in gully formation and evolution. We suggest that illumination analysis like the presented here could help to evaluate those hypotheses, relating the insolation over recent periods with geomorphological pieces of evidence and the possible presence of subsurface ice, or thermal weathering of rocks.

5. Conclusions

We presented a code that simulates illumination conditions on Mars' surface using DTMs. Our code can create accurate illumination maps, which can be translated into energy budget maps, in short computational times.

The accuracy of near-surface illumination predictions is highly dependent on the local topography and, specially, on the DTM resolution.

Hence, DTMs of high resolution are needed to investigate illumination conditions in small areas, but this implies larger computational times (Acton, 1996; Gläser et al., 2014). Nevertheless, the approach presented here proved to be good enough to analyze small areas with high resolution at short time cost.

Further work will include an analysis of the slopes in order to make corrections in the energy received, by each pixel, with respect to the Sun's incidence angle and surface reflections. Moreover, an improvement on the result could be done by incorporating light reflections of the surrounding terrains and ambient light. Also, for energy studies an atmospheric model must be incorporated specially when working in long time scales due to probability of dust storms.

In conclusion, this routine presents a new approach to investigate future landing areas for rovers and assist on solar sustained habitats on Mars as well as geomorphological processes.

Acknowledgments

This work was financed by UBACYT 20020130300015BA. This is the R-253 contribution of the Instituto de Estudios Andinos Don Pablo Groeber, University of Buenos Aires, Conicet. We would like to thank the editors and an anonymous reviewer for the improvements on the manuscript. The code presented here can be accessed through <https://zenodo.org/record/1215719>. HIRISE DTMS can be accessed using <https://www.uahirise.org/>.

References

- Acton, C. H. Jr. (1996). Ancillary data services of NASA's navigation and ancillary information facility. *Planetary and Space Science*, *44*(1), 65–70. [https://doi.org/10.1016/0032-0633\(95\)00107-7](https://doi.org/10.1016/0032-0633(95)00107-7)
- Allison, M. (1997). Accurate analytic representations of solar time and seasons on Mars with applications to the pathfinder/surveyor missions. *Geophysical Research Letters*, *24*(16), 1967–1970. <https://doi.org/10.1029/97GL01950>
- Allison, M., & McEwen, M. (2000). A post-pathfinder evaluation of aerocentric solar coordinates with improved timing recipes for Mars seasonal/diurnal climate studies. *Planetary and Space Science*, *48*(2-3), 215–235. [https://doi.org/10.1016/S0032-0633\(99\)00092-6](https://doi.org/10.1016/S0032-0633(99)00092-6)
- Bussey, D. B. J., McGovern, J. A., Spudis, P. D., Neish, C. D., Noda, H., Ishihara, Y., & Sorensen, S. A. (2010). Illumination conditions of the South Pole of the Moon derived using Kaguya topography. *Icarus*, *208*(2), 558–564.
- Bussey, D. B. J., Spudis, P. D., & Robinson, M. S. (1999). Illumination conditions at the lunar south pole. *Geophysical Research Letters*, *26*(9), 1187–1190. <https://doi.org/10.1029/1999GL900213>
- Carpenter, J. D., Fisackerly, R., De Rosa, D., & Houdou, B. (2012). Scientific preparations for lunar exploration with the European lunar lander. *Planetary and Space Science*, *74*, 208–223.
- Chen-Chen, H., Pérez-Hoyos, S., & Sánchez-Lavega, A. (2019). Dust particle size and optical depth on Mars retrieved by the MSL navigation cameras. *Icarus*, *319*, 43–57. <https://doi.org/10.1016/j.icarus.2018.09.010>
- De Rosa, D., Bussey, B., Cahill, J. T., Lutz, T., Crawford, I. A., Hackwill, T., et al. (2012). Characterisation of potential landing sites for the European space agency's lunar Lander project. *Planetary and Space Science*, *74*, 224–246.
- Dundas, C. M., Bramson, A. M., Ojha, L., Wray, J. J., Mellon, M. T., Byrne, S., & Holt, J. W. (2018). Exposed subsurface ice sheets in the Martian mid-latitudes. *Science*, *359*(6372), 199–201. <https://doi.org/10.1126/science.aao1619>
- Evans, W., Kirkpatrick, D., & Townsend, G. (2001). Right-triangulated irregular networks. *Algorithmica*, *30*(2), 264–286.
- García-Chevesich, P., Bendek, E., Pizarro, R., Valdes-Pineda, R., Gonzalez, D., Bown, H., et al. (2017). Weathering processes on Martian craters: Implications on recurring slope lineae and the location of liquid water. *Open Journal of Modern Hydrology*, *7*, 245–256.
- Gläser, P., Scholten, F., De Rosa, D., Marco Figuera, R., Oberst, J., Mazarico, E., et al. (2014). Illumination conditions at the lunar south pole using high resolution digital terrain models from LOLA. *Icarus*, *243*, 78–90.
- Kirk, R. L. M., Holmberg, I. M., Kesztelyi, L. P., Redding, B. L., Delamere, W. A., Gallagher, D., et al. (2008). Ultrahigh resolution topographic mapping of Mars with MRO HiRISE stereo images: Meter-scale slopes of candidate Phoenix landing sites. *Journal of Geophysical Research*, *113*, E00A24. <https://doi.org/10.1029/2007JE003000>
- Kolb, K. J., Pelletier, J. D., & McEwen, A. S. (2010). Modeling the formation of bright slope deposits associated with gullies in Hale crater, Mars: Implications for recent liquid water. *Icarus*, *205*-1, 113–137.
- Marco Figuera, R., Gläser, P., Oberst, J., & de Rosa, D. (2014). Calculation of illumination conditions at the lunar south pole—Parallel programming approach. EPSC abstracts (Vol. 9).
- Margot, J. L., Campbell, D. B., Jurgens, R. F., & Slade, M. A. (1999). Topography of the lunar poles from radar interferometry: A survey of cold trap locations. *Science*, *284*(5420), 1658–1660. <https://doi.org/10.1126/science.284.5420.1658>
- Marks, D., Elmore, P., Blain, C. A., Bourgeois, B., Petry, F., & Ferrini, V. (2017). A variable resolution right TIN approach for gridded oceanographic data. *Computers & Geosciences*, *109*, 59–66. <https://doi.org/10.1016/j.cageo.2017.07.008>
- Mazarico, E., Neumann, G. A., Smith, D. E., Zuber, M. T., & Torrence, M. H. (2011). Illumination conditions of the lunar polar regions using LOLA topography. *Icarus*, *211*(2), 1066–1081. <https://doi.org/10.1016/j.icarus.2010.10.030>
- McEwen, A. S., Eliason, E. M., Bergstrom, J. W., Bridges, N. T., Hansen, C. J., Delamere, W. A., et al. (2007). Mars reconnaissance orbiter's High Resolution Imaging Science Experiment (HiRISE). *Journal of Geophysical Research*, *112*, E05S02. <https://doi.org/10.1029/2005JE002605>
- MEPAG (2015). Mars scientific goals, objectives, investigations, and priorities: 2015. In V. Hamilton (Ed.), *The Mars Exploration Program Analysis Group (MEPAG)* (74 pp.). Retrieved from <http://mepag.nasa.gov/reports.cfm>
- Noda, H., Araki, H., Goossens, S., Ishihara, Y., Matsumoto, K., Tazawa, S., et al. (2008). Illumination conditions at the lunar polar regions by KAGUYA (SELENE) laser altimeter. *Geophysical Research Letters*, *35*, L24203. <https://doi.org/10.1029/2008GL035692>
- Núñez, J. I., Barnouin, O. S., Murchie, S. L., Seelos, F. P., McGovern, J. A., Seelos, K. D., & Buczkowski, D. L. (2016). New insights into gully formation on Mars: Constraints from composition as seen by MRO/CRISM. *Geophysical Research Letters*, *43*, 8893–8902. <https://doi.org/10.1002/2016GL068956>
- Raack, J., Reiss, D., Appéré, T., Vincendon, M., Ruesch, O., & Hiesinger, H. (2015). Present-day seasonal gully activity in a south polar pit (Sisyphi Cavi) on Mars. *Icarus*, *251*, 226–243. <https://doi.org/10.1016/j.icarus.2014.03.040>
- Sherwood, B. (2017). Space architecture for MoonVillage. *Acta Astronautica*, *139*, 396–406. <https://doi.org/10.1016/j.actaastro.2017.07.019>
- Snyder, J. P. (1987). Map projections: A working manual. Geological Survey (U.S.).
- Speyerer, E. J., & Robinson, M. S. (2013). Persistently illuminated regions at the lunar poles: Ideal sites for future exploration. *Icarus*, *222*(1), 122–136. <https://doi.org/10.1016/j.icarus.2012.10.010>
- Stenzel, C., Weiss, L., & Rohr, T. (2018). Sustainable challenges on the moon. *Current Opinion in Green and Sustainable Chemistry*, *9*, 8–12. <https://doi.org/10.1016/j.cogsc.2017.10.002>

- Strausberg, M. J., Wang, H., Richardson, M. I., Ewald, S. P., & Toigo, A. D. (2005). Observations of initiation and evolution of the 2001 Mars global dust storm. *Journal of Geophysical Research*, *110*, E02006. <https://doi.org/10.1029/2004JE002361>
- Wu, Y., & Hapke, B. (2018). Spectroscopic observations of the moon at the lunar surface. *Earth and Planetary Science Letters*, *484*, 145–153. <https://doi.org/10.1016/j.epsl.2017.12.003>